

## Effects of runner design and pressurization on the microstructure of a high-pressure die cast Mg–3.0Nd–0.3Zn–0.6Zr alloy

Tongtong Zhang, Wenbo Yu, Chaosheng Ma, Yuqi Zhou, and Shoumei Xiong

Cite this article as:

Tongtong Zhang, Wenbo Yu, Chaosheng Ma, Yuqi Zhou, and Shoumei Xiong, Effects of runner design and pressurization on the microstructure of a high-pressure die cast Mg–3.0Nd–0.3Zn–0.6Zr alloy, *Int. J. Miner. Metall. Mater.*, 29(2022), No. 7, pp. 1310-1316. <https://doi.org/10.1007/s12613-021-2386-z>

View the article online at [SpringerLink](#) or [IJMMM Webpage](#).

### Articles you may be interested in

Hong-xiang Li, Shi-kai Qin, Ying-zhong Ma, Jian Wang, Yun-jin Liu, and Ji-shan Zhang, [Effects of Zn content on the microstructure and the mechanical and corrosion properties of as-cast low-alloyed Mg–Zn–Ca alloys](#), *Int. J. Miner. Metall. Mater.*, 25(2018), No. 7, pp. 800-809. <https://doi.org/10.1007/s12613-018-1628-1>

Chong Lin, Shu-sen Wu, Shu-lin Lü, Ping An, and He-bao Wu, [Effects of high-pressure rheo-squeeze casting on the Fe-rich phases and mechanical properties of Al-17Si-\(1,1.5\)Fe alloys](#), *Int. J. Miner. Metall. Mater.*, 25(2018), No. 9, pp. 1018-1026. <https://doi.org/10.1007/s12613-018-1652-1>

Zhuo Yi, Wen-zhi Fu, Ming-zhe Li, Rui Li, Liang Zhao, and Li-yan Wang, [Numerical simulation and experimental verification of a novel double-layered split die for high-pressure apparatus used for synthesizing superhard materials](#), *Int. J. Miner. Metall. Mater.*, 26(2019), No. 3, pp. 377-385. <https://doi.org/10.1007/s12613-019-1747-3>

Zhi-yong Xue, Yue-juan Ren, Wen-bo Luo, Yu Ren, Ping Xu, and Chao Xu, [Microstructure evolution and mechanical properties of a large-sized ingot of Mg-9Gd-3Y-1.5Zn-0.5Zr \(wt%\) alloy after a lower-temperature homogenization treatment](#), *Int. J. Miner. Metall. Mater.*, 24(2017), No. 3, pp. 271-279. <https://doi.org/10.1007/s12613-017-1405-6>

Cheng-bin Cai, Xiao-jing Xu, Jin-dong Huang, Shi-hao Ju, Qing Ding, and Cheng-song Wang, [Effect of pre-recovery on microstructure and properties of rolled Al-12.18Zn-3.31Mg-1.43Cu-0.20Zr-0.04Sr aluminum alloy](#), *Int. J. Miner. Metall. Mater.*, 26(2019), No. 2, pp. 241-250. <https://doi.org/10.1007/s12613-019-1729-5>

A. V. Kolygin, V. E. Bazhenov, R. S. Khasenova, A. A. Komissarov, A. I. Bazlov, and V. A. Bautin, [Effects of small additions of Zn on the microstructure, mechanical properties and corrosion resistance of WE43B Mg alloys](#), *Int. J. Miner. Metall. Mater.*, 26(2019), No. 7, pp. 858-868. <https://doi.org/10.1007/s12613-019-1801-1>



IJMMM WeChat



QQ author group

# Effects of runner design and pressurization on the microstructure of a high-pressure die cast Mg–3.0Nd–0.3Zn–0.6Zr alloy

Tongtong Zhang<sup>1</sup>), Wenbo Yu<sup>1</sup>),<sup>✉</sup>, Chaosheng Ma<sup>1</sup>), Yuqi Zhou<sup>2</sup>), and Shoumei Xiong<sup>2</sup>),<sup>✉</sup>

1) Center of Materials Science and Engineering, School of Mechanical and Electronic Control Engineering, Beijing Jiaotong University, Beijing 100044, China

2) School of Materials Science and Engineering, Tsinghua University, Beijing 100084, China

(Received: 7 September 2021; revised: 21 November 2021; accepted: 22 November 2021)

**Abstract:** To clarify the relationship between externally solidified crystals (ESCs) and other defects, e.g., defect bands and pores, two dimensional (2D) and three dimensional (3D) characterization methods were adopted to analyze castings produced using a modified ingate system equipped with and without an ESC collector. The reduction of ESCs strongly reduced defect band width and shrinkage pore quantity. By reducing the quantity and size of ESCs, net-shrinkage pores were transformed into isolated island-shrinkage pores. We determined via statistical analysis that the mechanical properties of high pressure die castings were strongly related to the size and fraction of the ESCs rather than porosity volume. The reduction of ESCs also caused tensile transgranular fracture modes to transform into intergranular fracture modes. Additionally, casting pressurization strongly reduced pore morphology, volume, and size.

**Keywords:** high-pressure die casting; externally solidified crystals; porosity; 3D reconstruction; runner design

## 1. Introduction

High pressure die casting (HPDC) is the typical method for producing thin-wall magnesium alloy castings due to its high formation accuracy, high efficiency, and minor post-processing requirements [1–2]. However, defects, e.g., pores, defect bands, and externally solidified crystals (ESCs), are often found in HPDC castings, which can be detrimental to mechanical performance [3–5].

Many studies have been carried out to investigate the formation of these defects and their influence on the mechanical performances of castings. For example, Weiler *et al.* [6] reported that the local area fraction of porosity was the main detrimental factor in tensile tests. Lee *et al.* [7–8] showed that ductility was correlated to the area fraction of porosity measured in a fracture surface and not with the average volume fraction of porosity in a three dimensional (3D) microstructure. Thus, porosity is an important factor that can affect the mechanical properties of castings. The formation of pores and defect bands are closely related to ESCs. ESCs are large-size grains that are pre-nucleated and grown in a short sleeve [9–10]. At fast slow-shot speeds, shear stress is produced when ESCs enter the cavity with molten metal, which causes the rotation of the ESCs and the formation of defect bands [11]. Insufficient melt feeding causes the formation of complex aggregated pores between ESCs in defect bands [12]. Accumulated ESCs continue to grow in casting centers and produce shrinkage pores due to lower melt feeding capabilities [13]. Yu *et al.* [14] reported that defect band width was

strongly correlated with the size and quantities of ESCs in AZ91D castings. Additionally, Li *et al.* [15–16] reported that defect bands with high porosities and complex morphologies acted as crack initiation sites, which facilitated crack propagation to the center and surface of a specimen.

It is clear that ESCs are strongly correlated with the porosity and defect bands in HPDC castings. Different methods have been adopted to optimize the microstructure of castings. Faster slow-shots can reduce the size and quantity of ESCs in castings at the risk of flow turbulence during plunger movement and shorter vacuum times [14,17]. However, more gas pores appear in these castings, which reduces the mechanical performance of the castings [18]. Alternatively, studies have been performed to improve microstructures through mold modification. Lee *et al.* [19] reduced pore volumes in final castings through overflow system optimization. Since stress can break ESCs when melts pass through ingates, Gunasegaram *et al.* [20] and Li *et al.* [13] successfully reduced ESC quantities by increasing the shear stress produced through a modified ingate system.

Recently, Zhou *et al.* [21] discovered that runners equipped with ESC collectors efficiently collected ESCs, which led to a more refined microstructure in a Mg–3.0Nd–0.3Zn–0.6Zr alloy. However, the correlation between the pore morphology and ESCs influenced by ESC collector was not investigated. 3D reconstruction methods have been used to characterize the 3D morphology of pores and their correlation with high-pressure die-casting process parameters [22–23]. For example, using a combination of two dimen-

✉ Corresponding authors: Wenbo Yu E-mail: wbyu@bjtu.edu.cn; Shoumei Xiong E-mail: smxiong@tsinghua.edu.cn

sional (2D) and 3D characterization methods, Ma *et al.* [24] determined shrinkage pores co-existed with ESCs in an HP-DC AE44 alloy. Furthermore, the liquid feeding performance can reduce porosity during melt solidification, and the effect of solidification pressure was studied for an HPCD process with an ingate runner and ESC collector. Here we employed 2D and 3D characterization methods to elucidate the correlation between pore morphology and ESCs.

## 2. Experimental

An Mg–3.0Nd–0.3Zn–0.6Zr alloy was selected and subsequently was cast using a Toyo TOYO-BD-350V5 cold chamber die-casting machine under vacuum. The chemical composition of the Mg–3.0Nd–0.3Zn–0.6Zr alloy is shown in Table 1. As shown in Fig. 1(a) and (b), ESCs first nucleate

and grow near the shot sleeve wall. An ESC collector was introduced at both sides of the ingate runner. For comparison, Fig. 1(c) and (d) shows the enlarged runner equipped without and with the ESC collector. During the HPDC process, the melting temperature, mold temperature, low slow-shot speed, and fast slow-shot speed were set as 700°C, 150°C, 0.1 m/s, and 2 m/s, respectively. The whole length and diameter of the shot sleeve were 340 and 70 mm, respectively. Additional details about three HPDC processes are summarized in Table 2.

**Table 1.** Chemical composition of the Mg–3.0Nd–0.3Zn–0.6Zr alloy

						wt%
Nd	Zr	Zn	Al	Ca	Fe	Mg
2.86	0.595	0.256	0.046	0.029	0.003	Bal

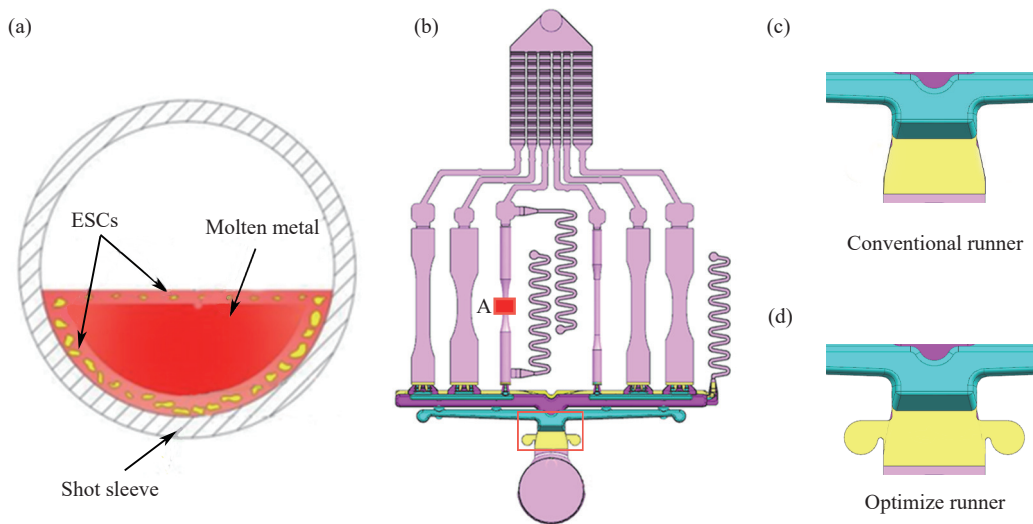


**Fig. 1.** (a) ESC nucleation position, (b) casting configuration, (c) conventional runner, and (d) optimized runner with the ESC collector.

**Table 2.** Parameters of three designed vacuum-assisted HPDC processes

Sample	Low slow-shot speed / ( $\text{m}\cdot\text{s}^{-1}$ )	Fast slow-shot speed / ( $\text{m}\cdot\text{s}^{-1}$ )	ESC collector	Solidification pressure / MPa
Without-E	0.1	2.0	No	79
With-E-P	0.1	2.0	Yes	79
Without-P	0.1	2.0	Yes	No

Specimens analyzed via scanning electron microscopy were taken from location “A” as marked in Fig. 1(b). To reconstruct 3D structures, synchrotron X-ray micro-tomography was performed at the BL13W1 line station of the Shanghai Synchrotron Radiation Facility, China. The X-ray energy of the synchrotron was 30 keV. A YAG:Ge scintillator screen equipped with a 2048 × 2048 pixel camera was used to convert X-rays to visible light. An inverse filter projection algorithm with the PITRE software was used to reconstruct 2D projections into 3D structures. Finally, the Avizo software was used to process the reconstructed data.

Tensile tests were performed on a WDW-3020 electron universal testing machine at room temperature (25°C), with a 1 mm/min displacement speed. Mechanical properties such as yield strength, ultimate tensile strength, and elongation of

six tensile specimens were evaluated.

## 3. Results

Fig. 2 shows the 2D and 3D morphologies of HPDC Mg–3.0Nd–0.3Zn–0.6Zr magnesium alloy casting produced without ESC collector (without-E). As shown in Fig. 2(a), the microstructure was composed of  $\alpha$ -Mg, ESCs, and  $\text{Mg}_{12}\text{Nd}$  phases located at  $\alpha$ -Mg grain boundaries and pores. Similar to HPDC AZ91D castings [14], the top and front views of the 3D reconstruction shown in Fig. 2(b) and (c) show that central pores were surrounded by ring-shaped accumulated pores (termed defect bands). Enlarged regions, labeled as I (skin layer), II (defect band zone), and III (center zone) in Fig. 2(b) and (c), are shown in Fig. 2(d)–(f). Small

gas pores (round) and island-shrinkage pores were observed in the skin layer. Large-size contiguous net-shrinkage pores and small gas pores were found in the defect band. Gas pores, gas-shrinkage pores (a round pore connected by an irregular shrinkage pore), and a large amount of isolated net-shrinkage and island-shrinkage pores appeared in the center zone.

Fig. 3 shows the 3D porosity distribution and morphologies of HPDC castings fabricated under three different condi-

tions. Under casting pressurization, the porosity was distributed with a spiral-staggered shape along the liquid flow direction, as shown in Fig. 3(a<sub>1</sub>) and (a<sub>2</sub>) and Fig. 3(b<sub>1</sub>) and (b<sub>2</sub>). The continuous spiral-staggered lines (defect bands) became disconnected when the ESC collector was introduced into the runner design. Without casting pressurization, the pores became more dispersed and the spiral-staggered lines disappeared (Fig. 3(c<sub>1</sub>) and (c<sub>2</sub>)). Lines were removed in the recon-

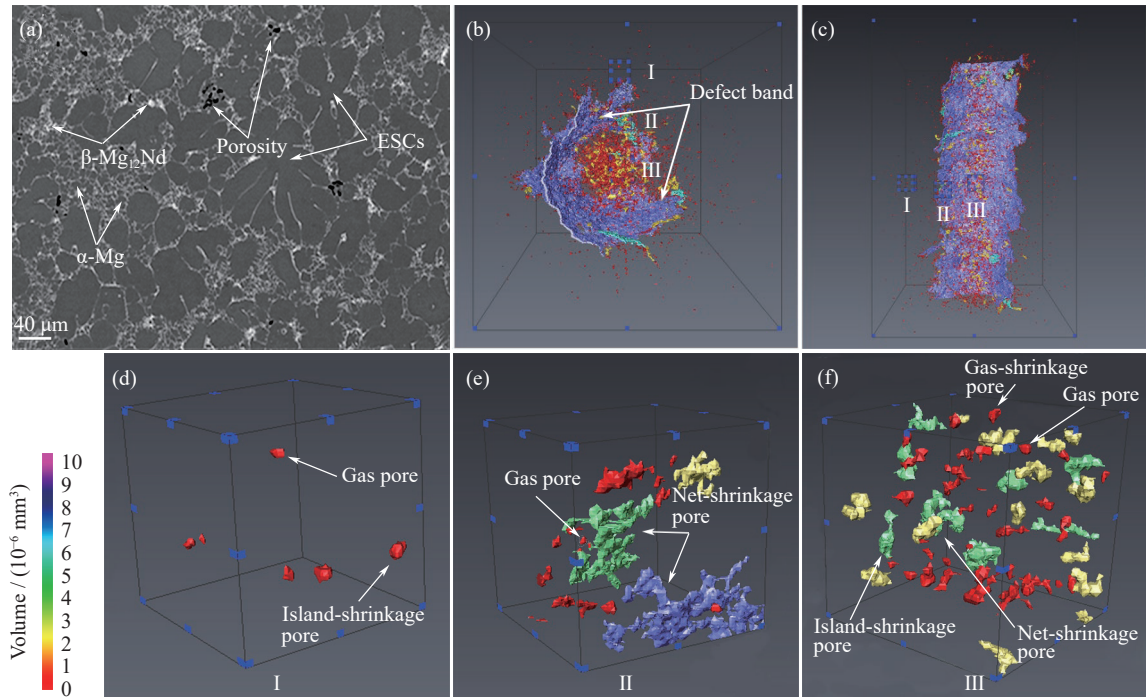


Fig. 2. (a) Back-scattered electron microscopy image of an Mg-3.0Nd-0.3Zn-0.6Zr alloy produced without ESC collector. 3D reconstruction (b) top view, (c) side view, and (d-f) pore morphologies observed in the three areas marked in (b) and (c).

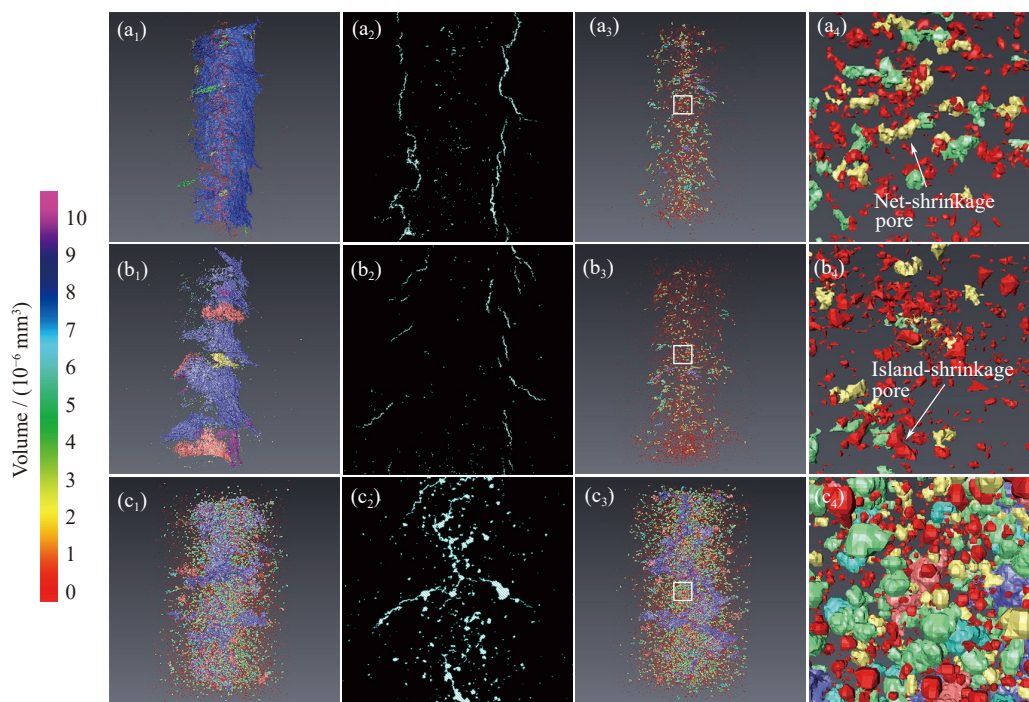
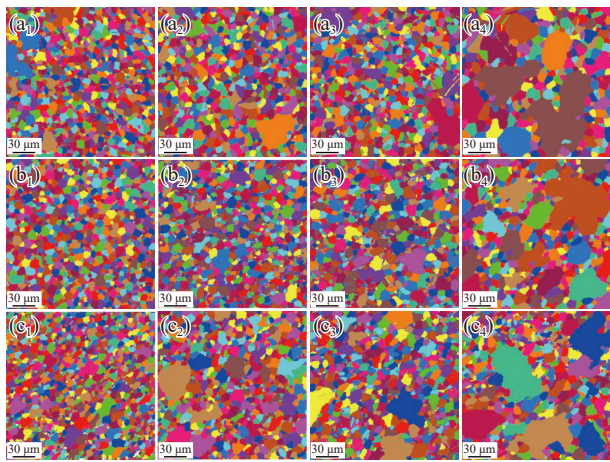


Fig. 3. (a<sub>1</sub>, b<sub>1</sub>, c<sub>1</sub>) 3D morphologies of specimens corresponding to without ESC collector, with ESC collector and solidification pressurization, and without solidification pressurization, respectively. (a<sub>2</sub>, b<sub>2</sub>, c<sub>2</sub>) Axial sections along the metal flow direction. (a<sub>3</sub>, b<sub>3</sub>, c<sub>3</sub>) 3D morphologies after line removal from (a<sub>2</sub>, b<sub>2</sub>, c<sub>2</sub>). (a<sub>4</sub>, b<sub>4</sub>, c<sub>4</sub>) Enlarged view of the areas marked in (a<sub>3</sub>, b<sub>3</sub>, c<sub>3</sub>).

structured images for clarity. The size and quantities of net-shrinkage pores were significantly reduced in the center zone with the introduction of the ESC collector, while more island-shrinkage pores appeared (Fig. 3(a<sub>3</sub>) and (a<sub>4</sub>)) and Fig. 3(b<sub>3</sub>) and (b<sub>4</sub>)). Without solidification pressurization, large gas pores and mixed net-island-shrinkage pores appeared (Fig. 3(c<sub>3</sub>) and (c<sub>4</sub>)).

The electron back scattered diffraction (EBSD) analysis of a scanning area of  $260\ \mu\text{m} \times 260\ \mu\text{m}$  in the skin layers, transition areas, and central zones of the three as-cast Mg–3.0Nd–0.3Zn–0.6Zr specimens is shown in Fig. 4. Calculated corresponding area percentages and grain sizes of the ESCs of the three areas are given in Fig. 5. The area fraction and aver-



**Fig. 4.** EBSD analysis of the skin layer (left column), transition zone (middle two columns), and center zone (right column): (a<sub>1</sub>–a<sub>4</sub>) without the ESC collector; (b<sub>1</sub>–b<sub>4</sub>) with the ESC collector and solidification pressurization; (c<sub>1</sub>–c<sub>4</sub>) without solidification pressurization. Boundaries between grains with a misorientation greater than 15° are marked by blue lines. Green lines mark boundaries with misorientations between 5° and 15°. Different colors represent different grain orientations.

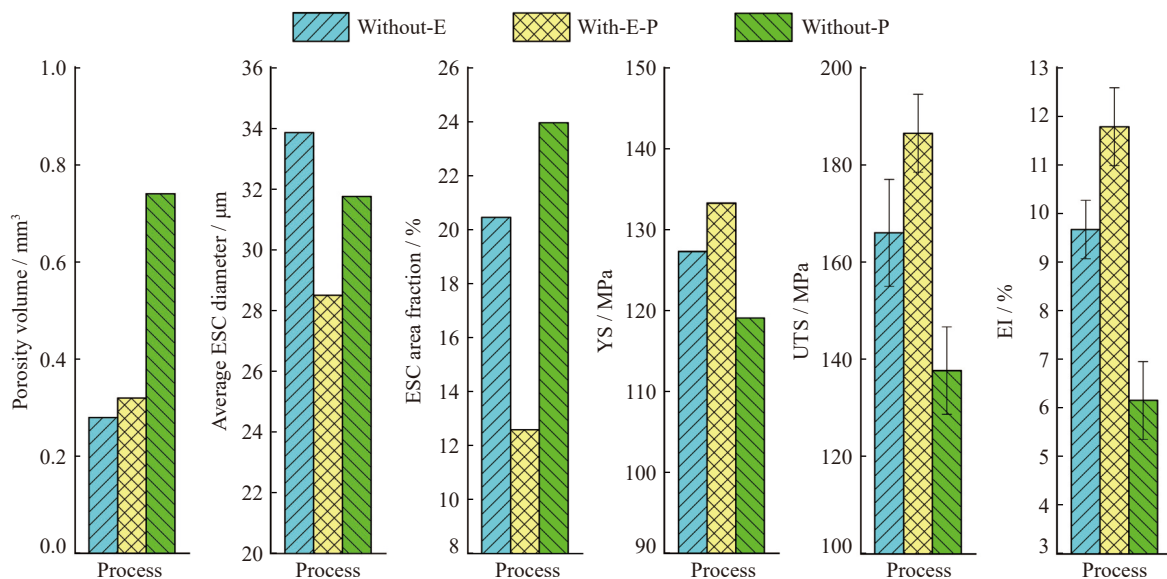


**Fig. 6.** Quantification of the porosity volume, average ESC diameter, ESCs area fraction, yield strength (YS), ultimate tensile strength (UTS), and elongation index (EI) of castings fabricated by the three designed processes. The dimension of the statistics is  $500 \times 500 \times 780\ \text{pixels}^3$  with a volume of  $53.55\ \text{mm}^3$ .

age size of the ESCs, from the skin layers to the center zones, increased linearly in the three as-cast specimens, and the slope of the curves increased sharply in the central zones. As shown in Fig. 4(a<sub>1</sub>)–(a<sub>4</sub>), Fig. 4(b<sub>1</sub>)–(b<sub>4</sub>), and Fig. 5, the introduction of a runner design reduced the area fraction and average size of the ESCs, with values of 7% and 8 μm for each position. Without pressurization (Fig. 4(b<sub>1</sub>)–(b<sub>4</sub>), Fig. 4(c<sub>1</sub>)–(c<sub>4</sub>), and Fig. 5), the area fraction and average size of the ESCs increased for each position. The average size of α-Mg also increased due to a decrease in the interfacial heat transfer coefficient and a deceleration of the solidification rate, which increased the growth time of α-Mg [25].

## 4. Discussion

As shown in Fig. 6, porosity volume significantly increased from  $0.321$  to  $0.745\ \text{mm}^3$ . This difference in volume indicates that pressurization can be used to optimize liquid feeding performance during melt solidification. The average diameters and particularly the area fractions of the ESCs sig-

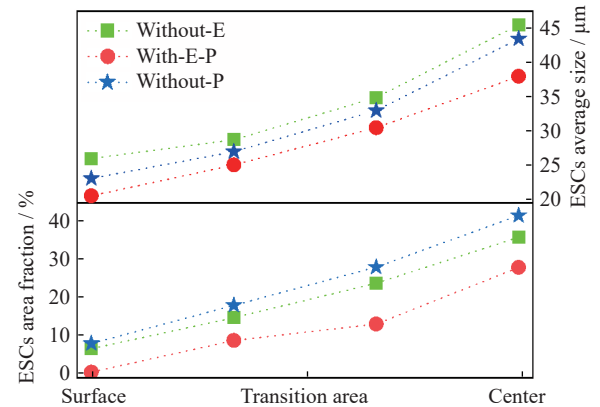


**Fig. 5.** Statistics of area percentages and grain sizes of ESCs at different distances from the surface to the center.

nificantly decreased with the introduction of ESC collectors. Fig. 7 shows the ESC distribution at four different positions of the ingate runner equipped with the ESC collector. The quantity and size of the ESCs significantly decreased when the melt flow passed by the ESC collector (Fig. 7(a) and (b)). Additionally, more ESCs appeared inside of the ESC collectors (Fig. 7(c) and (d)). These results demonstrated that the collector efficiently collected ESCs. Shrinkage pores form at ESC boundaries due to solidification contraction [22]. Here, a greater amount of larger island-shrinkage pores appeared from the skin layer to the center zone. Thus, gaps among ESCs decreased due to ESC reduction in the final castings due to the ESC collector. As reported by Li *et al.* [22] and Yu *et al.* [14], net-shrinkage pores are typically produced among connected ESCs because gaps among ESCs are difficult to fill. The quantity and size of net-shrinkage pores were reduced and dispersed in castings with the introduction of ESC collectors (Fig. 3(a<sub>1</sub>)–(a<sub>3</sub>) and (b<sub>1</sub>)–(b<sub>3</sub>)). Fewer ESCs remained in the melt, and thus a higher fraction of liquid metal was in the die cavity, which increased shrinkage in the cavity during melt solidification. Thus, the porosity volume increased from 0.271 to 0.321 mm<sup>3</sup>, with a corresponding percentage increase from 0.164% to 0.194%, when the ESC collector was introduced in the conventional runner. The specimen produced with the ESC collector exhibited better mechanical performance compared with the specimen produced without the ESC collector under the same casting pressurization (Fig. 6). Song *et al.* [26] and Sun *et al.* [27] reported that the strength and elongation of HPDC magnesium alloys are related to porosity volume fractions and pore sizes. We dis-

covered that the mechanical performance was strongly related to the ESC fraction instead of the porosity volume (Fig. 6 and Fig. 3). Furthermore, it was reported that ductility was related to the area fraction of porosity on the fracture surface and not the average 3D volume fraction of porosity [18]. More pores appeared on the fracture surface of the specimen produced without the ESC collector compared with the specimen with the ESC collector (Figs. 8(a) and 9(a)).

The tensile fracture surfaces of HPDC bars produced without and with ESC collectors are shown in Figs. 8 and 9, respectively. For both specimens, cracks initiated from the center of the bars as pores were mainly accumulated there. These cracks and pores then propagated to the circumference

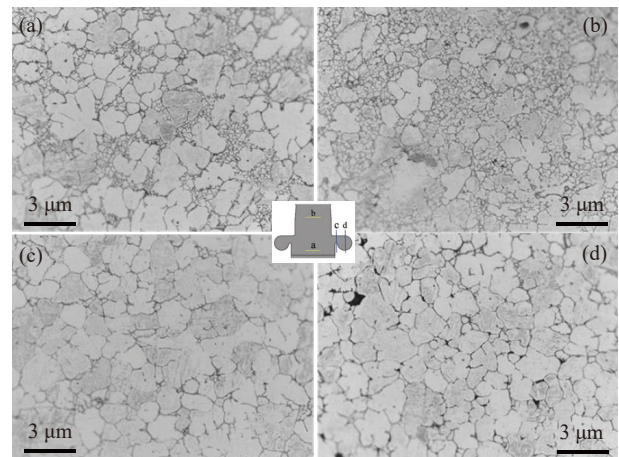


Fig. 7. Microstructure morphologies of corresponding positions of the specimen.

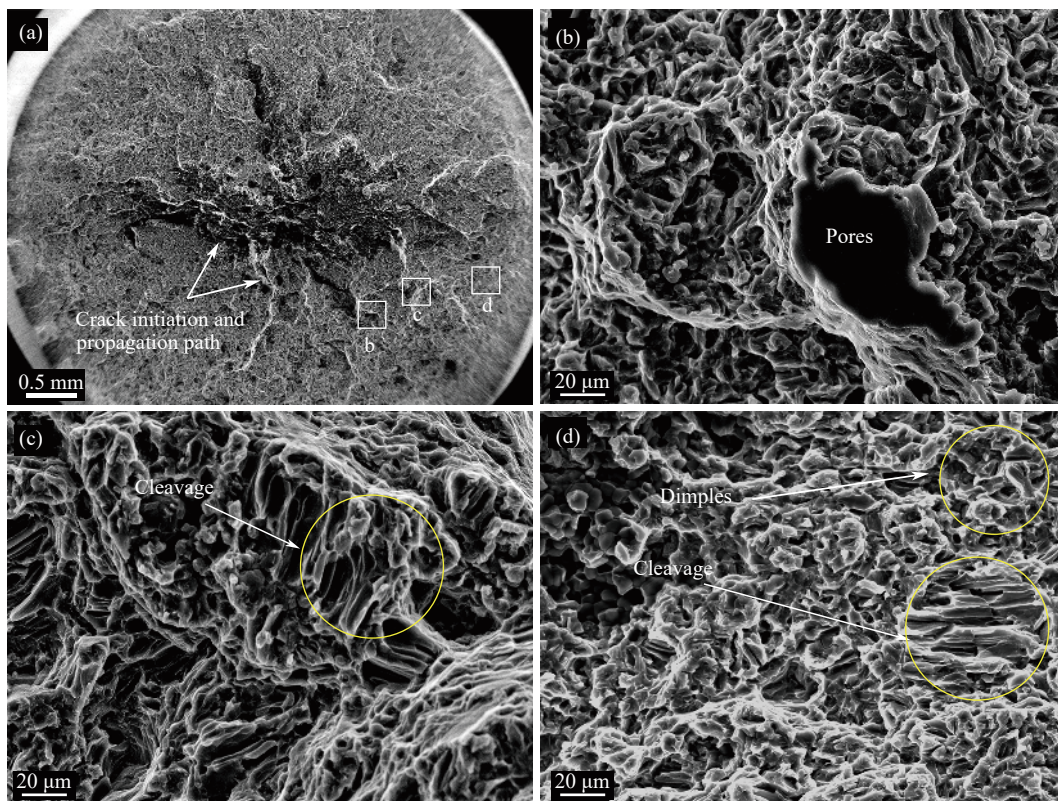
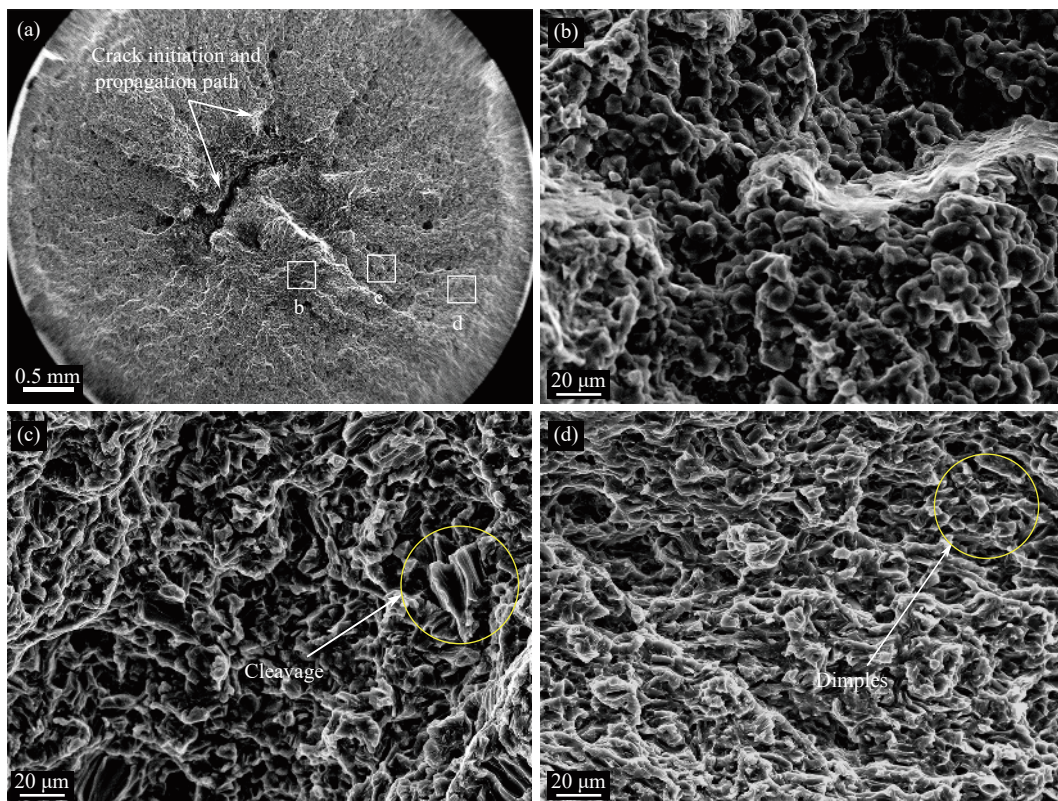


Fig. 8. Tensile fracture without the ESC collector: (a) the overall morphology of the fracture and (b–d) enlarged marked areas of the surface in (a).



**Fig. 9.** Tensile fracture with the ESC collector: (a) the overall morphology of the fracture and (b–d) enlarged areas from the surface in (a).

edge of the radial structures for the specimens produced without the ESC collector. Flatter fractures were found in the bar obtained with the ESC collector. Li *et al.* [16] reported that transgranular fractures generally produced a flat fracture morphology, while intergranular fractures produced a rough fracture morphology. Tearing ridges resulted from the evolution of slip bands where ESCs were dominant [15]. Herein, in comparison with the fracture surface of casting produced without ESCs collectors shown in Fig. 8, Fig. 9 shows less tearing ridges caused by the lower quantity ESCs due to the ESCs collectors. Connected net-shrinkage pores (Fig. 3(a<sub>1</sub>)–(a<sub>4</sub>)) facilitate crack propagation. However, these cracks were deflected by the island-shrinkage pores in the specimen produced with the ESC collector.

## 5. Conclusion

In this study, we investigated the influence of casting pressurization and mold runner design on the 2D and 3D microstructure of HPCD castings. Our results confirm that accumulated ESCs favor the formation of net-shrinkage pores in castings. Pressurization strongly reduced the porosity volume through the optimization of the liquid feeding performance during melt solidification. Runner collectors efficiently reduced the quantity and size of ESCs with 7% and 8 μm in castings. Furthermore, continuous staggered lines in defect bands were broken, and net-shrinkage pores in defect and center zones were significantly reduced. Tensile tests showed that transgranular fractures accompanied with less ESC cleavage occurred in castings produced with the ESC collect-

or, while intergranular fractures accompanied with more ESCs occurred in castings produced without the ESC collector. The mechanical properties of HPDC castings were related to ESC fractions rather than porosity volumes.

## Acknowledgements

This work was financially supported by the National Natural Science Foundation of China (No. 52175284) and the State Key Lab of Advanced Metals and Materials in University of Science and Technology Beijing (No. 2021-ZD08).

## Conflict of Interest

The authors have no competing interests to declare that are relevant to the content of this article.

## References

- [1] J. Rong, W.L. Xiao, X.Q. Zhao, C.L. Ma, H.M. Liao, D.L. He, M. Chen, M. Huang, and C. Huang, High thermal conductivity and high strength magnesium alloy for high pressure die cast ultrathin-walled component, *Int. J. Miner. Metall. Mater.*, 29(2022), No. 1, p. 88.
- [2] G.H. Wu, C.L. Wang, M. Sun, and W.J. Ding, Recent developments and applications on high-performance cast magnesium rare-earth alloys, *J. Magnes. Alloys*, 9(2021), No. 1, p. 1.
- [3] K.K. Wang, Y.L. Kang, and K. Zhang, Effects of rare earth elements on the microstructure and properties of magnesium alloy AZ91D, *J. Univ. Sci. Technol. Beijing*, 9(2002), No. 5, p. 363.
- [4] H.I. Laukli, L. Amberg, and O. Lohne, Effects of grain refiner additions on the grain structures in HPDC A356 castings, *Int. J.*

- Cast Met. Res.*, 18(2005), No. 2, p. 65.
- [5] Z.M. Sheggaf, R. Ahmad, M.B.A. Asmael, and A.M.M. Elasad, Solidification, microstructure, and mechanical properties of the as-cast ZRE1 magnesium alloy with different praseodymium contents, *Int. J. Miner. Metall. Mater.*, 24(2017), No. 11, p. 1306.
- [6] J.P. Weiler, J.T. Wood, R.J. Klassen, E. Maire, R. Berkmortel, and G. Wang, Relationship between internal porosity and fracture strength of die-cast magnesium AM60B alloy, *Mater. Sci. Eng. A*, 395(2005), No. 1-2, p. 315.
- [7] S.G. Lee, G.R. Patel, A.M. Gokhale, A. Sreeranganathan, and M.F. Horstemeyer, Variability in the tensile ductility of high-pressure die-cast AM50 Mg-alloy, *Scripta Mater.*, 53(2005), No. 7, p. 851.
- [8] S.G. Lee, G.R. Patel, A.M. Gokhale, A. Sreeranganathan, and M.F. Horstemeyer, Quantitative fractographic analysis of variability in the tensile ductility of high-pressure die-cast AE44 Mg-alloy, *Mater. Sci. Eng. A*, 427(2006), No. 1-2, p. 255.
- [9] W.B. Yu, Y.Y. Cao, X.B. Li, Z.P. Guo, and S.M. Xiong, Determination of interfacial heat transfer behavior at the metal/shot sleeve of high pressure die casting process of AZ91D alloy, *J. Mater. Sci. Technol.*, 33(2017), No. 1, p. 52.
- [10] R. Helenius, O. Lohne, L. Arnberg, and H.I. Laukli, The heat transfer during filling of a high-pressure die-casting shot sleeve, *Mater. Sci. Eng. A*, 413-414(2005), p. 52.
- [11] W.B. Yu, Y.Y. Cao, Z.P. Guo, and S.M. Xiong, Development and application of inverse heat transfer model between liquid metal and shot sleeve in high pressure die casting process under non-shooting condition, *China Foundry*, 13(2016), No. 4, p. 269.
- [12] S. Barbagallo, Shrinkage porosity in thin walled AM60 HPDC magnesium alloy U-shaped box, *Int. J. Cast Met. Res.*, 17(2004), No. 6, p. 364.
- [13] X.B. Li, Z.P. Guo, and S.M. Xiong, Influence of melt flow on the formation of defect band in high pressure die casting of AZ91D magnesium alloy, *Mater. Charact.*, 129(2017), p. 344.
- [14] W.B. Yu, C.S. Ma, Y.H. Ma, and S.M. Xiong, Correlation of 3D defect-band morphologies and mechanical properties in high pressure die casting magnesium alloy, *J. Mater. Process. Technol.*, 288(2021), art. No. 116853.
- [15] X. Li, S.M. Xiong, and Z. Guo, On the tensile failure induced by defect band in high pressure die casting of AM60B magnesium alloy, *Mater. Sci. Eng. A*, 674(2016), p. 687.
- [16] X. Li, S.M. Xiong, and Z. Guo, Failure behavior of high pressure die casting AZ91D magnesium alloy, *Mater. Sci. Eng. A*, 672(2016), p. 216.
- [17] Q.L. Wang and S.M. Xiong, Effect of multi-step slow shot speed on microstructure of vacuum die cast AZ91D magnesium alloy, *Trans. Nonferrous Met. Soc. China*, 25(2015), No. 2, p. 375.
- [18] S.G. Lee and A.M. Gokhale, Formation of gas induced shrinkage porosity in Mg-alloy high-pressure die-castings, *Scripta Mater.*, 55(2006), No. 4, p. 387.
- [19] B.D. Lee, U.H. Baek, and J.W. Han, Optimization of gating system design for die casting of thin magnesium alloy-based multi-cavity LCD housings, *J. Mater. Eng. Perform.*, 21(2012), No. 9, p. 1893.
- [20] D.R. Gunasegaram, M. Givord, R.G. O'Donnell, and B.R. Finnin, Improvements engineered in UTS and elongation of aluminum alloy high pressure die castings through the alteration of runner geometry and plunger velocity, *Mater. Sci. Eng. A*, 559(2013), p. 276.
- [21] Y. Zhou, Z. Guo, and S.M. Xiong, Effect of runner design on the externally solidified crystals in vacuum die-cast Mg-3.0Nd-0.3Zn-0.6Zr alloy, *J. Mater. Process. Technol.*, 267(2019), p. 366.
- [22] X. Li, S.M. Xiong, and Z. Guo, Improved mechanical properties in vacuum-assist high-pressure die casting of AZ91D alloy, *J. Mater. Process. Technol.*, 231(2016), p. 1.
- [23] Z.X. Li, D.J. Li, W.K. Zhou, B. Hu, X.F. Zhao, J.Y. Wang, M. Qin, J.K. Xu, and X.Q. Zeng, Characterization on the formation of porosity and tensile properties prediction in die casting Mg alloys, *J. Magnes. Alloys*, (2021). DOI: [10.1016/j.jma.2020.12.006](https://doi.org/10.1016/j.jma.2020.12.006)
- [24] C.S. Ma, W.B. Yu, T.T. Zhang, Z.H. Zhang, Y.H. Ma, and S.M. Xiong, The effect of slow shot speed and casting pressure on the 3D microstructure of high pressure die casting AE44 magnesium alloy, *J. Magnes. Alloys*, (2021). DOI: [10.1016/j.jma.2021.09.011](https://doi.org/10.1016/j.jma.2021.09.011)
- [25] Z.P. Guo, S.M. Xiong, M. Li, and J. Allison, Relationship between metal-die interfacial heat transfer coefficient and casting solidification rate in high pressure die casting process, *Acta Metall. Sin.*, 45(2009), No. 1, p. 102.
- [26] J. Song, S.M. Xiong, M. Li, and J. Allison, The correlation between microstructure and mechanical properties of high-pressure die-cast AM50 alloy, *J. Alloys Compd.*, 477(2009), No. 1-2, p. 863.
- [27] X. Sun, K.S. Choi, and D.S. Li, Predicting the influence of pore characteristics on ductility of thin-walled high pressure die casting magnesium, *Mater. Sci. Eng. A*, 572(2013), p. 45.